Although a wholly magnetospheric (power-law) origin for the observed x-ray emission is plausible, the neutral hydrogen column density [$N_H \sim 1.5 \times 10^{21}$ cm^{-2}; (8)] implied by the model is higher than expected from the pulsar's previously assumed location in the Gum nebula. The Gum nebula is believed to be ~500 pc distant, with a depth of several hundred pc (5).

However, the value of N_H is consistent with the usual average of 10 neutral hydrogen atoms for every free electron along the line of sight. Our revised distance estimate places PSR J0737-3039A/B beyond the Gum nebula, implying that the measured value for N_H is not discrepant. It also increases the estimated x-ray luminosity by a factor of 5, but the revised value for a power-law fit (1.2×10^{31} erg s^{-1}) remains consistent with known relations between pulsar spin-down luminosity and x-ray luminosity (18). Hence, our result supports a power-law model of magnetospheric origin (from pulsar A) for the bulk of the x-ray emission from PSR J0737-3039A/B.

The discovery of PSR J0737-3039A led to a marked upward revision in the estimated Galactic merger rate of DNS systems (19), although uncertainty over the characteristics of recycled pulsars means that the true value of the merger rate remains poorly constrained. Specifically, the distribution of recycled pulsar luminosities is generally extrapolated from the entire pulsar population (19) even though it (along with the distributions of pulse shape and beaming fraction) appears to differ from the distribution for slower pulsars (20). Our revised distance shows that the radio luminosity of PSR J0737-3039A is a factor of 5 greater than previously assumed. If this revision were to markedly influence the recycled pulsar luminosity function, then the assumed space density of DNS systems would be reduced, with a corresponding impact on DNS merger rates estimations.

Finally, we used the measured transverse velocity for PSR J0737-3039A/B (24^{+9}_{-6} km s^{-1}) to constrain models of the formation of the system. After subtracting estimates of the peculiar motion of the solar system and Galactic rotation (21), we measure a transverse velocity in local standard of rest of 9^{+6}_{-3} km s^{-1}. This is comparable to the unadjusted value of 10 km s^{-1} presented in (3), and is within the range of transverse velocities expected for the massive stars that are DNS progenitors [~20 km s^{-1}; (22)]. Because the transverse velocity of PSR J0737-3039A/B is so low, if the system received a large velocity kick at birth, it must have a large radial velocity. However, there are no observational methods available to determine the radial velocity in a DNS system.

Because of the accurate measurement of its Shapiro delay, PSR J0737-3039A/B is known to lie edge-on (3). If the only kick it received was provided by the loss of binding energy during the supernova explosion, the resultant three-dimensional space velocity should be on the order of ~ 50 km s^{-1}, estimated from the system's observed eccentricity and orbital velocity (23).

This space velocity would be constrained to the plane of the orbit. From simple geometry, the probability of observing a transverse velocity less than 10 km s^{-1} is about one in eight, which is small, but not unreasonable. Conversely, if the double pulsar had received a large kick (24), the odds of observing such a low transverse velocity become increasingly remote. Not only would the radial velocity have to be increasingly large, but the inclination angle of the system must not be altered by the kick. Hence, our transverse velocity results reinforce those of (3) and are consistent with the interpretation of (25), who argue for almost no mass loss and kick in the case of PSR J0737-3039A/B.

The implication of low kick velocities in PSR J0737-3039A/B–like systems offers a possible, albeit speculative, explanation for the formation of PSR J1903+0327, a heavy, highly recycled millisecond pulsar (mass 1.8 solar masses, period 2.15 ms) with a main-sequence companion of 1 solar mass (26). The orbit of such a pulsar should have been highly circularized during the mass-transfer phase (27). However, PSR J1903+0327 possesses an intermediate orbital eccentricity ($e = 0.44$).

A formation mechanism for PSR J1903+0327 has been suggested in which a triple system experiences a white dwarf–neutron star coalescence (28). However, a coalescing DNS system such as PSR J0737-3039A/B could also create a PSR J1903+0327–like pulsar. Thus, given the low velocity of PSR J0737-3039A/B, an alternative formation mechanism for PSR J1903+0327 involves a triple system containing a close DNS binary and a main-sequence star.

References and Notes
1. M. Burgay et al., Nature **426**, 531 (2003).
2. A. G. Lyne et al., Science **303**, 1153 (2004).
3. M. Kramer et al., Science **314**, 97 (2006).
4. J. H. Taylor, J. M. Cordes, Astrophys. J. **411**, 674 (1993).
5. J. M. Cordes, T. J. W. Lazio, http://arxiv.org/abs/astro-ph/0207156 (2002).
6. W. F. Brisken, S. E. Thorsett, A. Golden, W. M. Goss, Astrophys. J. **593**, L89 (2003).
7. M. A. McLaughlin et al., Astrophys. J. **605**, L41 (2004).
8. A. Possenti et al., Astrophys. J. **680**, 654 (2008).
9. Information on materials and methods is available on Science Online.
10. I. S. Shklovskii, Sov. Astron. **13**, 562 (1970).
11. T. Damour, J. H. Taylor, Astrophys. J. **366**, 501 (1991).
12. W. S. Dias, J. R. D. Lépine, Astrophys. J. **629**, 825 (2005).
13. J. Holmberg, C. Flynn, Mon. Not. R. Astron. Soc. **352**, 440 (2004).
14. S. Chatterjee, B. M. Gaensler, A. Melatos, W. F. Brisken, B. W. Stappers, Astrophys. J. **670**, 1301 (2007).
15. A. Pellizzoni, A. Tiengo, A. De Luca, P. Esposito, S. Mereghetti, Astrophys. J. **679**, 664 (2008).
16. W. Becker, in Highly Energetic Physical Processes and Mechanisms for Emission from Astrophysical Plasmas, P. C. H. Martens, S. Tsuruta, M. A. Weber, Eds., vol. 195 of IAU Symposium (2000), p. 49.
17. M. Lyutikov, Mon. Not. R. Astron. Soc. **353**, 1095 (2004).
18. J. E. Grindlay et al., Astrophys. J. **581**, 470 (2002).
19. V. Kalogera et al., Astrophys. J. **601**, L179 (2004).
20. M. Kramer et al., Astrophys. J. **501**, 270 (1998).
21. F. Mignard, Astron. Astrophys. **354**, 522 (2000).
22. M. W. Feast, M. Shuttleworth, Mon. Not. R. Astron. Soc. **130**, 245 (1965).
23. A. Blaauw, Bull. Astron. Inst. Neth. **15**, 265 (1961).
24. B. Willems, J. Kaplan, T. Fragos, V. Kalogera, K. Belczynski, Phys. Rev. D Part. Fields Gravit. Cosmol. **74**, 043003 (2006).
25. T. Piran, N. J. Shaviv, Phys. Rev. Lett. **94**, 051102 (2005).
26. D. J. Champion et al., Science **320**, 1309 (2008).
27. M. A. Alpar, A. F. Cheng, M. A. Ruderman, J. Shaham, Nature **300**, 728 (1982).
28. E. P. J. van den Heuvel, Science **320**, 1298 (2008).
29. We acknowledge discussions with M. Kramer and E. van den Heuvel. A.T.D. is supported via a Swinburne University of Technology Chancellor's Research Scholarship and a Commonwealth Scientific and Industrial Research Organisation (CSIRO) postgraduate scholarship. The Long Baseline Array is part of the Australia Telescope, which is funded by the Commonwealth of Australia for operation as a National Facility managed by CSIRO.

Phase-Sensitive Observation of a Spin-Orbital Mott State in Sr$_2$IrO$_4$

B. J. Kim,[1,2]* H. Ohsumi,[3] T. Komesu,[3] S. Sakai,[3,4] T. Morita,[3,5] H. Takagi,[1,2]* T. Arima[3,6]

Measurement of the quantum-mechanical phase in quantum matter provides the most direct manifestation of the underlying abstract physics. We used resonant x-ray scattering to probe the relative phases of constituent atomic orbitals in an electronic wave function, which uncovers the unconventional Mott insulating state induced by relativistic spin-orbit coupling in the layered 5d transition metal oxide Sr$_2$IrO$_4$. A selection rule based on intra-atomic interference effects establishes a complex spin-orbital state represented by an effective total angular momentum = 1/2 quantum number, the phase of which can lead to a quantum topological state of matter.

Transition metal oxides (TMOs) with perovskite structure are hosts to many fascinating phenomena, including high-temperature superconductivity (1) and colossal magnetoresistance (2), in which the valence d-electron states are described in terms of crystal-field (CF) states: triply degenerate t_{2g} states (xy, yz, zx) and doubly degenerate e_g states ($x^2 - y^2$, $3z^2 - r^2$). These CF states are all pure real functions, so that when the degeneracy is re-

moved (e.g., by the Jahn-Teller effect), the orbital angular momentum is totally quenched. However, when the spin-orbit coupling (SOC) becomes effective, the CF states are mixed with complex phases, which may partially restore the orbital angular momentum in the t_{2g} manifold. This effect is particularly pronounced in TMOs with heavy 5d elements, where SOC is at least an order of magnitude larger than those of TMOs with 3d elements and can sometimes give rise to unconventional electronic states.

5d TMO Sr_2IrO_4 is a layered perovskite with low-spin d^5 configuration, in which five electrons are accommodated in almost triply degenerate t_{2g} orbitals. Metallic ground states are expected in 5d TMOs because of their characteristic wide bands and small Coulomb interactions as compared with those of 3d TMOs. Sr_2IrO_4, however, is known to be a magnetic insulator (3, 4). A recent study has shown that the strong SOC inherent to 5d TMOs can induce a Mott instability even in such a weakly correlated electron system (5), resulting in a localized state very different from the well-known spin $S = 1/2$ state for conventional Mott insulators, proposed to be an effective total angular momentum $J_{eff} = 1/2$ state in the strong SOC limit expressed as

$$|J_{eff} = 1/2, m_{J_{eff}} = \pm 1/2\rangle = \frac{1}{\sqrt{3}}(|xy, \mp\sigma\rangle \mp |yz, \pm\sigma\rangle + i|zx, \pm\sigma\rangle) \quad (1)$$
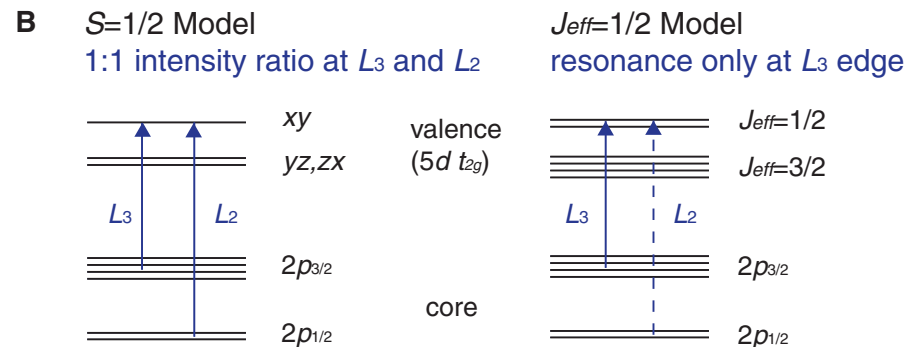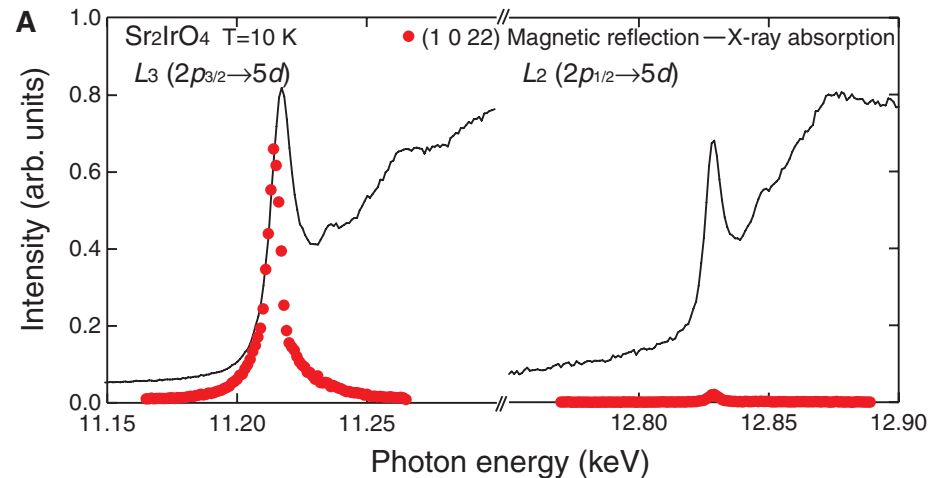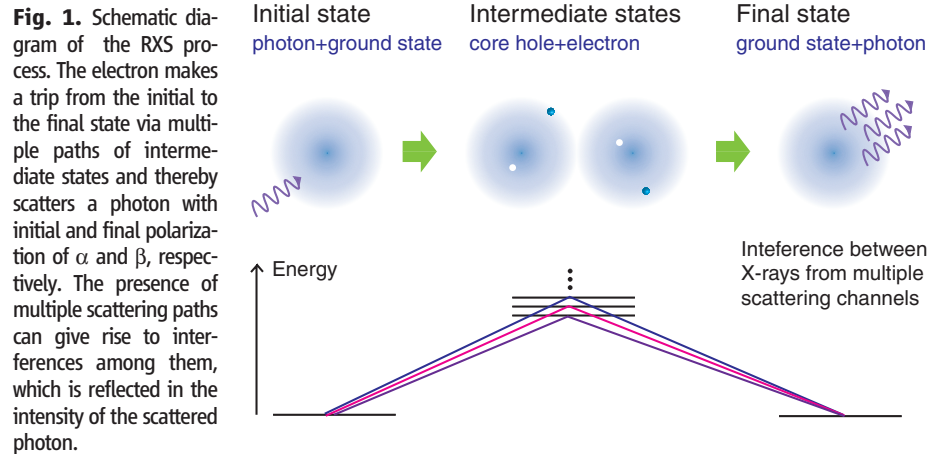
where m is the component of J_{eff} along the quantization axis and σ denotes the spin state. This state derives from the addition of $S = 1/2$ to the effective orbital angular momentum $L_{eff} = 1$, which consists of triply degenerate t_{2g} states but acts like the atomic $L = 1$ state with a minus sign; that is, $L_{eff} = -L$. As a result, $J_{eff} = 1/2$ has orbital moment parallel to spin (6). Note the characteristic equal mixture of xy, yz, and zx orbitals with complex number i involved in one of the factors and the mixed up-and-down spin states (7).

This realization of a Mott insulator with $J_{eff} = 1/2$ moment provides a new playground for correlated electron phenomena, because emergent physical properties that arise from it can be drastically different from those of the conventional Mott insulators. A prime example is when $J_{eff} = 1/2$ is realized in a honeycomb lattice structure where electrons hopping between $J_{eff} = 1/2$ states acquire complex phase; it generates a Berry phase leading to the recent prediction of

quantum spin-Hall effect at room temperature (8), and it also leads to the low-energy Hamiltonian of Kitaev model relevant for quantum computing (9). Experimental establishment of the $J_{eff} = 1/2$ state is thus an important step toward these physics, and the direct probe of complex phase in the wave function has been awaited. However, it is usually difficult to retrieve the phase in-

formation experimentally, because it is always the intensity, the square modulus of the wave function, that is measured; and thus a reference, with which the state under measurement can interfere, is required.

The resonant x-ray scattering (RXS) technique uses resonance effects at an x-ray absorption edge to selectively enhance the signal of

Fig. 1. Schematic diagram of the RXS process. The electron makes a trip from the initial to the final state via multiple paths of intermediate states and thereby scatters a photon with initial and final polarization of α and β, respectively. The presence of multiple scattering paths can give rise to interferences among them, which is reflected in the intensity of the scattered photon.

Fig. 2. Resonant enhancement of the magnetic reflection (1 0 22) at the L edge. (**A**) Solid lines are x-ray absorption spectra indicating the presence of Ir L_3 (2$p_{3/2}$) and L_2 (2$p_{1/2}$) edges around 11.22 and 12.83 keV. The dotted red lines represent the intensity of the magnetic (1 0 22) peak (Fig. 3C). Miller indices are defined with respect to the unit cell in Fig. 3A. (**B**) Calculation of x-ray scattering matrix elements expects equal resonant scattering intensities at L_3 and L_2 for the $S = 1/2$ model. For the $J_{eff} = 1/2$ model, in contrast, the resonant enhancement occurs only for the L_3 edge, and zero enhancement is expected at the L_2 edge.

[1]Department of Advanced Materials, University of Tokyo, Kashiwa 277-8561, Japan. [2]Magnetic Materials Laboratory, RIKEN Advanced Science Institute, Wako 351-0198, Japan. [3]RIKEN SPring-8 Center, Sayo 679-5148, Japan. [4]Department of Physical Science, Hiroshima University, Higashi-Hiroshima 739-8526, Japan. [5]Department of Physics, Kwansei-Gakuin University, Sanda 669-1337, Japan. [6]Institute of Multidisciplinary Research for Adavanced Materials, Tohoku University, Sendai 980-8577, Japan.

*To whom correspondence should be addressed. E-mail: bjkim6@gmail.com (B.J.K.); htakagi@k.u-tokyo.ac.jp (H.T.)

interest, and has become a powerful tool for investigating ordering phenomena (10, 11). So far, the emphasis has been seen only in the amplification of the signal. However, the RXS signal contains important information about the phase of the wave function for valence electrons, because RXS results from quantum interference between different scattering paths via intermediate states of a single site. The RXS process is described by the second-order process of electron-photon coupling perturbation, as schematically shown in Fig. 1, and its scattering amplitude $f_{\alpha\beta}$ from a single site is expressed under dipole approximation by

$$f_{\alpha\beta} = \sum_m \frac{m_e \omega_{im}^3}{\omega} \frac{\langle i|R_\beta|m\rangle\langle m|R_\alpha|i\rangle}{\hbar\omega - \hbar\omega_{im} + i\Gamma/2} \quad (2)$$

In this process, a photon with energy (h)ω is scattered by being virtually absorbed and emitted with polarizations α and β, respectively; and in the course of the process, an electron of mass m_e makes dipole transitions through position operators R_α and R_β from and to the initial state i, via all possible intermediate states m, collecting the phase factors associated with the intermediate states, weighted by some factors involving energy differences between the initial and intermediate states (h)ω_{im} and the lifetime broadening energy Γ. The interference between various scattering paths is directly reflected in the scattering intensities of the photon, and in this way the valence electronic states can be detected with phase sen-

sitivity. This process can be contrasted with that in x-ray absorption spectroscopy (XAS), which is a first-order process and measures only the amplitudes of the individual paths, or transition probabilities to various valence states.

We have applied this technique to explore unconventional electronic states produced by the strong SOC in Sr_2IrO_4. Sr_2IrO_4 is an ideal system in which to fully use this technique. The magnetic Bragg diffraction in magnetically ordered Sr_2IrO_4 comes essentially from scattering by Ir t_{2g} electrons, to which RXS using the L edge ($2p{\rightarrow}5d$) can be applied to examine the electronic states. The wavelength at the L edge of $5d$ Ir is as short as ~1 Å, in marked contrast to >10 Å for $3d$ elements. This short wavelength makes the detection of RXS signals much easier than in $3d$ TMOs, because there exists essentially no constraint from the wavelength in detecting the magnetic Bragg signal. Moreover, the low-spin $5d^5$ configuration, a one-hole state, greatly reduces the number of intermediate states and makes the calculation of scattering matrix elements tractable. The excitation to the t_{2g} state completely fills the manifold, and the remaining degrees of freedom reside only in the $2p$ core holes. Because the intermediate states are all degenerate in this case, the denominator factors involving energies and lifetimes of the intermediate states in Eq. 2 can drop out. A careful analysis of the scattering intensity can show that the wave function given by Eq. 1 represents the ground state in Sr_2IrO_4 (4).

Figure 2A shows the resonance enhancement of the magnetic reflection (1 0 22) at the L edge of a Sr_2IrO_4 single crystal (4), overlaid with XAS spectra to show the resonant edges. Whereas there is a huge enhancement of the magnetic reflection by a factor of ~10^2 at the L_3 edge, the resonance at L_2 is small, showing less than 1% of the intensity at L_3. The constructive interference at L_3 gives a large signal that allows the study of magnetic structure, whereas the destructive interference at the L_2 edge hardly contributes to the resonant enhancement.

To find out the necessary conditions for the hole state leading to the destructive interference at the L_2 edge, we calculate the scattering amplitudes. The most general wave function for the hole state in the t_{2g} manifold involves six basis states, which can be reduced by block-diagonalizing the spin-orbit Hamiltonian as

$$c_1|xy,+\sigma\rangle + c_2|yz,-\sigma\rangle + c_3|zx,-\sigma\rangle \quad (3)$$

With its time-reversed pair, they fully span the t_{2g} subspace. We neglect higher-order corrections such as small residual coupling between t_{2g} and e_g manifolds. In the limit of the tetragonal crystal field [$Q \equiv E(d_{xy}) - E(d_{yz,zx})$] due to the elongation of octahedra much larger than SOC (λ_{SO}) (that is, $Q \gg \lambda_{SO}$), the ground state will approach $c_1 = 1$ and $c_2 = c_3 = 0$ and become a $S = 1/2$ Mott insulator, whereas in the other limit of strong SOC, $Q \ll \lambda_{SO}$, c_i's will all be equal in magnitude, with c_1, c_2 pure real and c_3
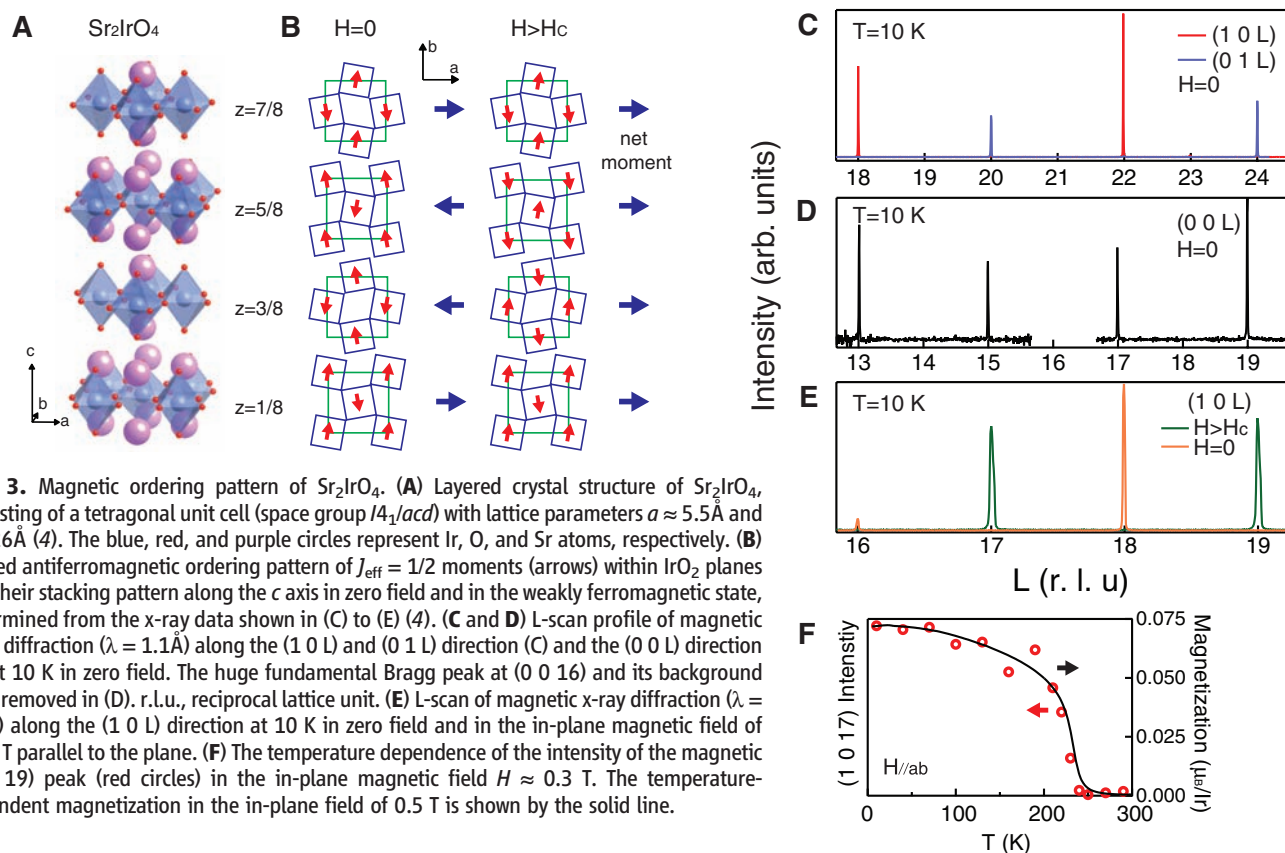
Fig. 3. Magnetic ordering pattern of Sr_2IrO_4. (**A**) Layered crystal structure of Sr_2IrO_4, consisting of a tetragonal unit cell (space group $I4_1/acd$) with lattice parameters $a \approx 5.5$Å and $c \approx 26$Å (4). The blue, red, and purple circles represent Ir, O, and Sr atoms, respectively. (**B**) Canted antiferromagnetic ordering pattern of $J_{eff} = 1/2$ moments (arrows) within IrO_2 planes and their stacking pattern along the c axis in zero field and in the weakly ferromagnetic state, determined from the x-ray data shown in (C) to (E) (4). (**C** and **D**) L-scan profile of magnetic x-ray diffraction ($\lambda = 1.1$Å) along the (1 0 L) and (0 1 L) direction (C) and the (0 0 L) direction (D) at 10 K in zero field. The huge fundamental Bragg peak at (0 0 16) and its background were removed in (D). r.l.u., reciprocal lattice unit. (**E**) L-scan of magnetic x-ray diffraction ($\lambda = 1.1$Å) along the (1 0 L) direction at 10 K in zero field and in the in-plane magnetic field of ≈ 0.3 T parallel to the plane. (**F**) The temperature dependence of the intensity of the magnetic (1 0 19) peak (red circles) in the in-plane magnetic field $H \approx 0.3$ T. The temperature-dependent magnetization in the in-plane field of 0.5 T is shown by the solid line.

pure imaginary as in Eq. 1. Calculation of $f_{\alpha\beta}$ for the L_2 edge using Eq. 5 gives

$$f_{\alpha\beta} =$$

$$\begin{pmatrix} (c_1 + ic_3)(c_1^* - ic_3^*) & (ic_1^* + c_3^*)(c_1 - c_2) & 0 \\ (-ic_1 + c_3)(c_1^* - c_2^*) & (c_1 - c_2)(c_1^* - c_2^*) & 0 \\ 0 & 0 & (c_2 + ic_3)(c_2^* - ic_3^*) \end{pmatrix}$$

(4)

Because the magnetic signal comes from the imaginary part of off-diagonal elements (12), the necessary condition for the vanishing intensity is

$$c_1 = c_2 \qquad \text{or} \qquad c_3 = ic_1 \qquad (5)$$

This condition places very stringent constraints on the allowed hole state and rules out all single-orbital $S = 1/2$ models. For the $S = 1/2$ case, the imaginary part of the off-diagonal elements does not vanish and equal resonant intensities are expected at the L_2 and L_3 edges (Fig. 2B). Given the constraints in Eq. 5, the scattering intensities at L_3 edge are calculated to be

$$I_{L_3} = \frac{1}{4}(Im(c_1 c_3^*))^2 \qquad \text{or}$$

$$I_{L_3} = \frac{1}{4}(Re(c_1^* c_2))^2 \qquad (6)$$

respectively. Thus, taking the phase convention $c_1 = 1$ without loss of generality, the resonant intensity at L_3 measures the imaginary part of c_3 relative to the real part of c_2, which is also a measure of orbital angular momentum. The large enhancement at L_3 necessarily implies that the yz orbital is out of phase with the zx orbital, the contrast between L_3 and L_2 being maximal when the relative phase is $\pi/2$. Taking the constraints of Eqs. 5 and 6 together, we conclude that the ground state is very close to the $J_{\rm eff} = 1/2$ limit ($c_1:c_2:c_3 = 1:1:i$), and the minute enhancement at L_2 edge shows the smallness of the deviation from the $J_{\rm eff} = 1/2$ limit coming from the factors not taken into account (13). The wave function in Eq. 2, representing $J_{\rm eff} = 1/2$, indeed gives zero off-diagonal elements in $f_{\alpha\beta}$ for L_2 and nonzero elements for the L_3 edge. This is a direct measurement of phase and provides evidence for the $J_{\rm eff} = 1/2$ state in Sr_2IrO_4.

Having identified the nature of the local moment, we now look at the global magnetic structure using the enhanced signal due to the resonance at the L_3 edge. Sr_2IrO_4 shows a metamagnetic transition below 240 K and, above the metamagnetic critical field H_C (≈ 0.2 T well below 240 K), shows weak ferromagnetism with a saturation moment of ≈ 0.1 μ_B/Ir (4). The origin of this field-induced weak ferromagnetism has remained unidentified, because the neutron diffraction data did not show any detectable indication of magnetic ordering (14). Our RXS results indicate that the magnetic structure of Sr_2IrO_4 is canted antiferromagnetic.

Figure 3A shows the crystal structure containing four IrO_2 layers in a unit cell, enlarged by superstructure from the rotational distortion of octahedra (14). Figure 3B shows the magnetic ordering pattern determined from the experiment

shown in Fig. 3, C to E. The arrows in Fig. 3B do not represent spins but $J_{\rm eff} = 1/2$ moments. In zero field, the magnetic reflections are observed at $(1\ 0\ 4n+2)$ and $(0\ 1\ 4n)$, which implies that the moments are aligned antiferromagnetically within a layer and the symmetry changes from tetragonal to orthorhombic (Fig. 3C). The canting of the moments yields a nonzero net moment within a layer, which orders in the up-down-down-up antiferromagnetic pattern along the c axis. This is evidenced by the presence of $(0\ 0\ odd)$ peaks shown (Fig. 3D). The width of the peak gives an estimate of interlayer correlation length of 100 c or 400 IrO_2 layers. When the magnetic field greater than H_C is applied, the peaks at $(1\ 0\ 4n+2)$ disappear and new peaks show up at $(1\ 0\ odd)$ (Fig. 3E), which implies that the net moments in the planes are aligned ferromagnetically to produce a macroscopic field. The temperature dependence of the scattering intensity in the weakly ferromagnetic state above H_C, shown in Fig. 3F, scales very well with that of the magnetization and confirms again the magnetic nature of the peaks.

Our study demonstrates that x-rays can be extended to a new level to probe even finer details of magnetic structure. Until now, only the intersite interference effects were used to study ordering phenomena over a length scale of many lattice sites. A quantitative analysis on the interference effects within a single site provides phase information on the constituent wave function of the electron responsible for the magnetism. This technique should find important applications in systems where complex phases give rise to novel physics.

References and Notes
1. J. G. Bednorz, K. A. Muller, *Z. Phys. B* **64**, 189 (1986).
2. For a review, see *Colossal Magnetoresistive Oxides*, Y. Tokura, Ed. (Gordon & Breach Science, New York, 2000).
3. G. Cao, J. Bolivar, S. McCall, J. E. Crow, R. P. Guertin, *Phys. Rev. B* **57**, R11039 (1998).
4. Materials and methods are available as supporting material on *Science* Online.
5. B. J. Kim *et al.*, *Phys. Rev. Lett.* **101**, 076402 (2008).
6. The parallel spin and orbital configuration are in accordance with Hund's third rule in the case of more than half-filled shell, despite its apparent contradiction implied by the $J_{\rm eff} = 1/2$ quantum number [see (5)].
7. This results in an orbital moment twice as large as that of spin,: $<L_z> = 2/3$ and $2<S_z> = 1/3$, with $<L_z> + 2<S_z> = 1$.
8. A. Shitade, H. Katsura, X.-L. Qi, S.-C. Zhang, N. Nagaosa, http://arxiv.org/abs/0809.1317.
9. G. Jackeli, G. Khaliullin, http://arxiv.org/abs/0809.4658.
10. Y. Murakami *et al.*, *Phys. Rev. Lett.* **81**, 582 (1998).
11. P. Abbamonte *et al.*, *Science* **297**, 581 (2002).
12. M. Blume, *Resonant Anomalous X-ray Scattering, Theory and Applications* (Elsevier Science, Amsterdam, 1994).
13. The small enhancement at L_2 can be explained by finite $10Dq$, which results in a small admixture of xy and $x^2 - y^2$ and small tetragonal splitting. It is not a priori obvious that $J_{\rm eff} = 1/2$ can be stabilized in the presence of the tetragonal crystal field, but the rotational distortion (Fig. 3A) acts in the opposite direction to lower the xy state, and this delicate balance may result in the $J_{\rm eff} = 1/2$ state (15).
14. M. K. Crawford *et al.*, *Phys. Rev. B* **49**, 9198 (1994).
15. B. J. Kim *et al.*, *Phys. Rev. Lett.* **97**, 106401 (2006).
16. The authors gratefully acknowledge discussions with C. Kim, J.-H. Park, S. Fujiyama, J. Matsuno, B. Smith, and G. Khaliullin; preliminary x-ray analysis by D. Hashizume; and continuous encouragement by M. Takata and T. Ishikawa. This work was partly supported by a Ministry of Education, Culture, Sports, Science and Technology (MEXT) Grant-in-Aid for Scientific Research (S) (19104008) and Grant-in-Aid for Scientific Research on Priority Areas "Novel States of Matter Induced by Frustration" (19052001 and 19052008).

The Earliest Horse Harnessing and Milking

Alan K. Outram,[1]* Natalie A. Stear,[2] Robin Bendrey,[3,7] Sandra Olsen,[4] Alexei Kasparov,[1,5] Victor Zaibert,[6] Nick Thorpe,[7] Richard P. Evershed[2]

Horse domestication revolutionized transport, communications, and warfare in prehistory, yet the identification of early domestication processes has been problematic. Here, we present three independent lines of evidence demonstrating domestication in the Eneolithic Botai Culture of Kazakhstan, dating to about 3500 B.C.E. Metrical analysis of horse metacarpals shows that Botai horses resemble Bronze Age domestic horses rather than Paleolithic wild horses from the same region. Pathological characteristics indicate that some Botai horses were bridled, perhaps ridden. Organic residue analysis, using $\delta^{13}C$ and δD values of fatty acids, reveals processing of mare's milk and carcass products in ceramics, indicating a developed domestic economy encompassing secondary products.

The domestication of the horse is associated with the spread of Indo-European languages and culture, bronze metallurgy, and specialized forms of warfare (1–3). Genetic studies of modern domestic horse breeds (*Equus caballus*) (4, 5) imply either multiple domestication events

or domestic stallions from a single original lineage being bred with captured local juvenile wild mares (6, 7), but fail to clearly identify when and where horse domestication first took place. A prime candidate for this locus is the Eurasian steppe, specifically the Botai culture, northern